

Fast Surface Dynamics of Metallic Glass Enable Superlatticelike Nanostructure Growth

L. Chen, C. R. Cao, J. A. Shi, Z. Lu, Y. T. Sun, P. Luo, L. Gu, H. Y. Bai, M. X. Pan,^{*} and W. H. Wang[†]

Institute of Physics, Chinese Academy of Sciences, Beijing 100190, People's Republic of China

(Received 10 July 2016; revised manuscript received 1 October 2016; published 5 January 2017)

Contrary to the formation of complicated polycrystals induced by general crystallization, a modulated superlatticelike nanostructure, which grows layer by layer from the surface to the interior of a $\text{Pd}_{40}\text{Ni}_{10}\text{Cu}_{30}\text{P}_{20}$ metallic glass, is observed via isothermal annealing below the glass transition temperature. The generation of the modulated nanostructure can be solely controlled by the annealing temperature, and it can be understood based on the fast dynamic and liquidlike behavior of the glass surface. The observations have implications for understanding the glassy surface dynamics and pave a way for the controllable fabrication of a unique and sophisticated nanostructure on a glass surface to realize the properties' modification.

DOI: 10.1103/PhysRevLett.118.016101

In glass, there is growing evidence that remarkable dynamic differences exist between the free surface and the corresponding bulk state [1–15], which were usually ignored for the strong bulk effects. However, with the decrease of glass size, the specific surface area increases dramatically. At a small length scale, the surface plays a crucial role in the dynamic behavior and properties of the entire glass system, as well as yielding numerous novel phenomena markedly different from those of the bulk [2,3]. Theoretical simulations and experimental investigations in both metallic and nonmetallic glasses confirm that the surface energy barrier is half that of the bulk [4,5]. Below T_g , the diffusivity of the surface is several orders of magnitude faster than that of the bulk [5–9], which can result in the formation of ultrastable glasses [10,11]. In organic glasses, the enhanced molecular mobility in a glassy surface has a vital influence on the fast surface crystallization, which was also observed in various other glasses recently [5,12–15]. The metallic glasses (MGs) with superior mechanical properties, attractive corrosion, and wear resistance [16–19] have promising potential for advanced applications such as microsized gears and cantilevers used in nano- or microelectromechanical systems [20,21]. Understanding the fundamental features of the surface is of utmost importance for the practical application of MGs on a small scale; however, the research on surface dynamics and novel phenomenon arising from the surface effects as well as their effects on the properties of MGs is still in its preliminary stage.

In this Letter, we study the surface dynamics behavior of a typical $\text{Pd}_{40}\text{Ni}_{10}\text{Cu}_{30}\text{P}_{20}$ metallic glass by using high resolution transmission electron microscopy (HRTEM), double spherical aberration-corrected high resolution scanning transmission electron microscopy (Cs STEM), and x-ray photoelectron spectroscopy (XPS). We observed the growth of a periodic superlatticelike nanostructure initiating on the surface via isothermal annealing below

T_g . These results might provide new insight into the relationship between the fast surface dynamics and the resulting crystallization behaviors and also pave a new way for the controllable growth of a unique and sophisticated nanostructure on the surface of MGs.

The $\text{Pd}_{40}\text{Ni}_{10}\text{Cu}_{30}\text{P}_{20}$ MG was selected for the experiments because of its outstanding oxidation resistance near T_g (=566 K). The sample preparation details can be found in the Supplemental Material [22]. The 3-mm-diameter MG rod was cut into slices with thickness of 1.5 mm, and the surfaces of the slices were mechanically polished to a shining mirror gloss until the visible scratches were removed. After polishing, the samples were ultrasonically cleaned in acetone and methanol and subsequently annealed in sealed quartz tubes under a reduced argon atmosphere ($\sim 2.0 \times 10^4$ Pa) to avoid oxidation and contamination during long-time isothermal treatment. The amorphous nature of the as-cast sample and crystallization behaviors of the annealed samples were examined by a Bruker D8 Advance x-ray diffractometer with $\text{Cu-K}\alpha$ radiation. The cross-section profiles of the annealed samples were examined with a Philips CM200 HRTEM and a JEOL-ARM200F Cs STEM, and the constituents at different depths were quantitatively determined by an ESCALAB 250 XPS.

To observe the impact of the surface dynamics, it is necessary for the temperature range to be below T_g [23]. Three different annealing temperatures ($T = 536, 546,$ and 556 K) were employed to investigate the temperature dependence of surface crystallization. The temperature fluctuation during the isothermal annealing was within 0.5 K. Figure 1 presents the XRD spectra of the samples at 546 K for 50 to 500 h. After 50-h annealing, a sharp peak arises at $2\theta = 39.6^\circ$, indicating that the MG starts to crystallize, which differs from a previous report that a primary crystalline phase with trigonal structure appears after annealing at 590 K (just above T_g) for about

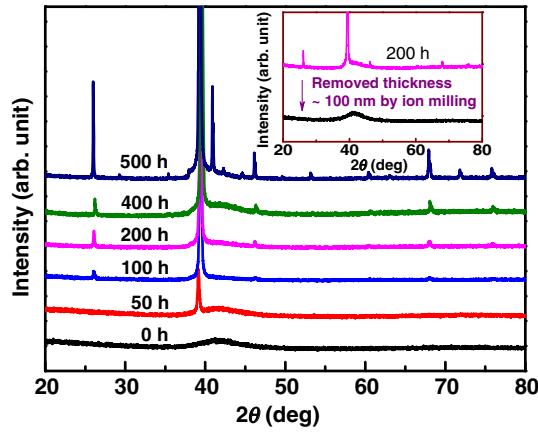


FIG. 1. XRD spectra of $\text{Pd}_{40}\text{Ni}_{10}\text{Cu}_{30}\text{P}_{20}$ MG annealed at 546 K ($=T_g - 20$ K) for different times. Inset: The surface crystalline layer (~ 100 nm thick) in MG annealed at 546 K for 200 h can be removed by ion milling.

30 h [24,25]. To lower the annealing temperature, the MG needs more time to overcome the energy barrier and to realize crystallization. With further annealing, more sharp diffraction peaks appear, such as the peaks at $2\theta = 27^\circ$, 46° , and 68° , which implies a single-crystal-like structure. Simultaneously, the intensities of these crystalline peaks become stronger with the annealing time. After removing the surface layer of ~ 100 nm of a 200-h annealed sample by ion milling (see the inset of Fig. 1), all crystallized XRD peaks disappear, demonstrating that crystallization only occurs at the surface of the MG, and the crystalline product phase grows from the surface into the interior of the bulk glass samples during the isothermal heat treatment.

Cs STEM and HRTEM were employed to examine the cross-sectional profile of the annealed MG samples prepared by the mechanical polishing and ion thinning techniques [26]. Figure 2(a) shows the cross-sectional Cs STEM view of the 200-h annealed sample. The rock-texture layer at the bottom right is Pt-C mixed glue to protect the surface from damage during the ion thinning process. After 200-h annealing, the initial disordered amorphous surface is replaced by a crystallized layer with a thickness of 95 nm, as labeled by the arrow. The insets of Fig. 2(a) show the selected area electron diffraction (SAED) patterns of the amorphous region, amorphous-crystalline interface zone, and crystalline surface layer zone (denoted as regions A, B, and C below), respectively. In region A, the halo ring confirms the amorphous nature of the inside of the annealed MG. The sharp and bright diffraction spots in region C indicate the single-crystal-like structure of the surface layer. For the same annealing process, regions B and C present totally different diffraction patterns compared with those of the interior zone of MG and conventional crystallized phases. Figure 2(b) shows the magnified image of region B in Fig. 2(a). Surprisingly, the crystalline phase in the surface layer is a periodic modulated structure with a period

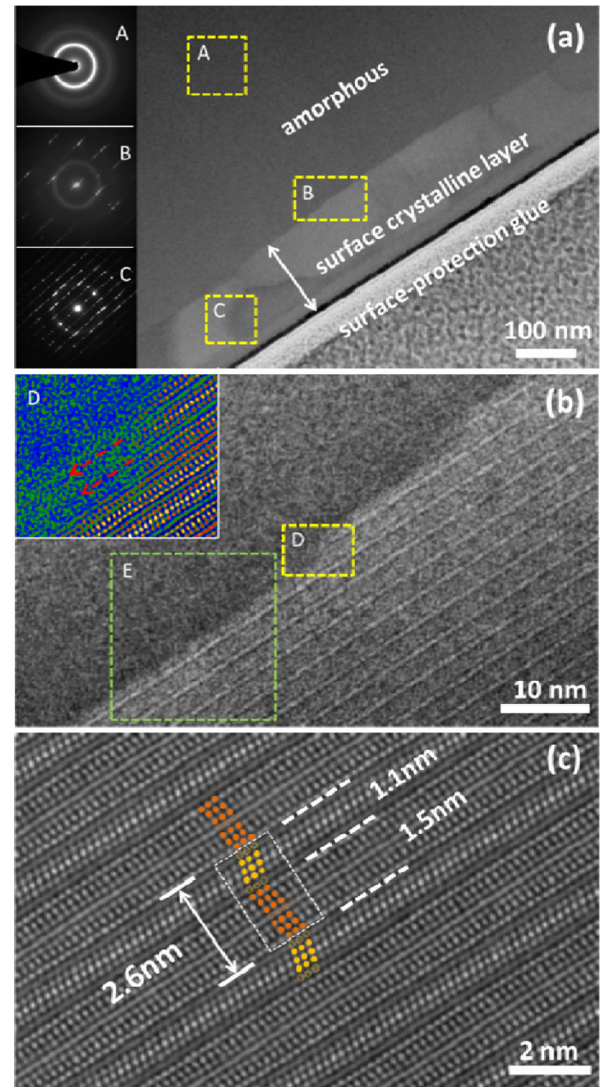


FIG. 2. (a) The cross-sectional Cs STEM view of the sample annealed at 546 K for 200 h. Insets: The SAED patterns of amorphous, amorphous-crystalline interface, and crystalline layer regions (denoted as regions A, B, C), respectively. (b) The magnified image of the selected amorphous-crystalline interface region B in (a). (c) The magnified image of the crystalline nanostructure.

of 2.6 nm [see Fig. 2(c)]. Figure 2(b) clearly exhibits that the modulated structure grows layer by layer from the surface to the interior, similar to the epitaxial growth mode. The inset of Fig. 2(b) shows area D at high magnification in color, where blue represents the background and the other colors reflect the atomic aggregation or rearrangement. After long-distance diffusion, the atoms self-assembly array along the newly grown crystalline layer and epitaxially grow towards the direction of the arrows. We have observed the similar superlattice-like nanostructures in other metallic glasses such as $\text{Zr}_{65}\text{Cu}_{15}\text{Ni}_{10}\text{Al}_{10}$ and $\text{Pd}_{40}\text{Ni}_{40}\text{P}_{20}$ (see Figs. S3 and S4 [22]), which confirm the generality of the observations.

The process of crystallization and the crystallized products are usually complicated because of the disordered structure and multicomponent in MGs [27–32]. The surface crystallization is accompanied by small intricate crystallites sporadically distributed on the surface, and the crystallized products are complicated polycrystalline phases [28]. The uniform growth of the periodic superlatticelike nanostructure on a glassy surface, to our best knowledge, has never been reported before. After annealing for 400 h, the surface “superlattice” layer was extended to 240 nm with the same period of 2.6 nm (see Fig. S1 [22]). The growing thickness (about 140 nm) of the surface crystalline layer during the latter 200 h is much larger than that of the initial 200 h. This is not only caused by the acceleration of crystallization but by a long incubation time before the onset of crystallization [24,25]. It is noted that the period of the superlattice remains unchanged, indicating that the growth process is more stable with the annealing time increasing. Fortuitously, the periodic structure is almost the same as the simulated self-organized alloy superlattice reported by Tersoff and co-workers [33]. However, the growth mechanisms of the two structures are essentially different. The simulated one requires a “step flow” surface to introduce a modulated strain field for the formation of the superlattice, while in our case, the initial surface morphology is not a staircase of atomic terraces but a disordered glassy structure. Another major distinction is that the growth direction in the simulation is along the lateral surface steps, whereas the superlattice in our case grows perpendicular to the surface. By carefully checking the atomic arrangement pattern of the modulated structure in Fig. 2(c), we find the existence of interlaced binary sublayers: the narrow one of 1.1 nm and the broader one of 1.5 nm, and, in the two sublayers, the atoms roughly array into two different orientations marked by dots. Since Cs STEM possesses atomic resolution, Fig. 2(c) asserts that the atomic arrangements in the sublayers are different; nevertheless, the chemical composition difference is still hard to distinguish.

To determine the constituents of the modulated nanostructure, the energy dispersive spectrometer (EDS) attached to Cs STEM was applied to analyze the distributions of elements at the $20 \times 20 \text{ nm}^2$ interface region *E* in Fig. 2(b). Figures 3(a)–3(d) are the corresponding elemental distribution graphs of Pd, Ni, Cu, and P, respectively. Different from the periodic streak pattern in region *E*, the distributions of Pd, Ni, Cu, and P in the modulated structure are homogeneous, implying the element compositions in the two sublayers are the same, and the modulated type is structural modulation. The composition of the crystalline phase is identified as $\text{Pd}_{34}\text{Ni}_{20}\text{Cu}_{33}\text{P}_{14}$ (the measuring error is $<5\%$), which is enriched in Cu and Ni, whereas it is depleted of P and Pd compared with the as-cast sample. These are totally different from the conventional crystallization in MGs, which usually intricately involves atomic long-distance diffusion and, consequently, pronounced compositional and structural

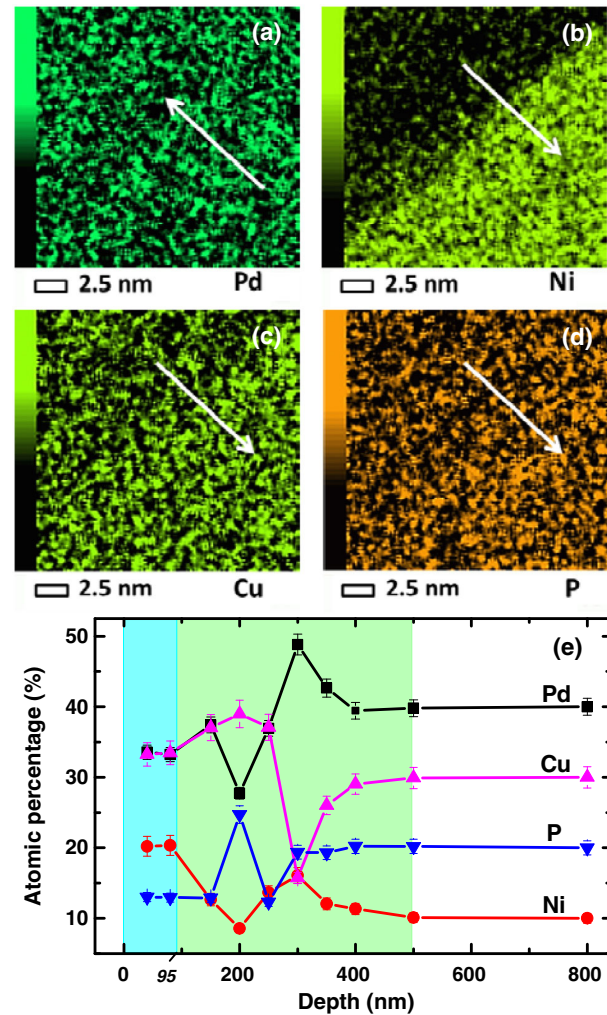


FIG. 3. (a)–(d) EDS elemental mapping of Pd, Ni, Cu, and P of region *E* in Fig. 2(b). The diffusion directions are labeled by arrows. (e) The atomic percentages of the components with depth varying. The constituents with different depths were quantitatively determined by XPS.

rearrangements, leading to the formation of complicated polycrystalline phases [27–32].

Recent work [5] shows that the bulk diffusivities of Pd are the slowest, and P is the fastest in PdNiCuP MG, which are estimated to be about $10^{-24} \text{ m}^2/\text{s}$ and $10^{-22} \text{ m}^2/\text{s}$ at 519 K (43 K below T_g), respectively. While the measured surface diffusion of the MG ($1.23 \times 10^{-16} \text{ m}^2/\text{s}$) is 5 and 8 orders of magnitude higher than the bulk diffusivities of P and Pd, respectively. We examined the atomic percentages of the components from the surface inwards to 800 nm deep by XPS (for details, see Ref. [22]), as shown in Fig. 3(e). The contents in the deep amorphous region are nearly the same to the as-cast MG. On the contrary, between the deep amorphous region and crystalline region, there exists a transition area about 400 nm thick (from 95 to 500 nm), where the percentage variations of the components change drastically. These results agree well with our

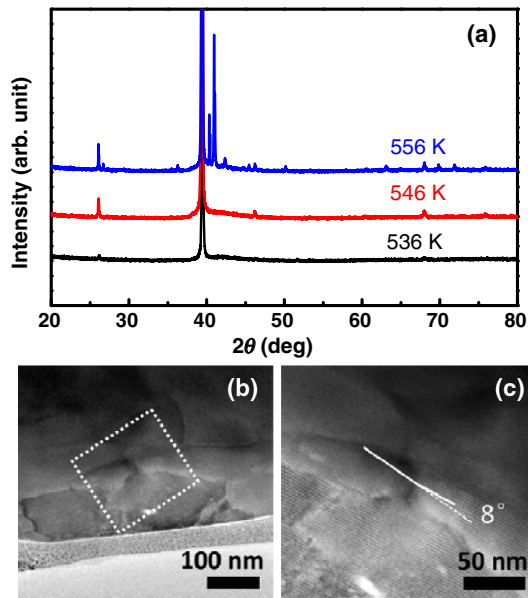


FIG. 4. (a) The XRD patterns of the samples annealed at different temperatures for 200 h. (b) The cross-sectional HRTEM image of the sample annealed at 556 K ($=T_g - 10$ K) for 200 h. (c) The magnified image of the selected zone in (b); the two grains show a small-angle misorientation of 8° .

previous report: for the extremely low bulk diffusivity, the atoms in the bulk can be regarded as frozen, whereas those close to the surface are still active. Near the frozen region, the contents of Cu and P decrease first then increase, indicating that they diffuse from the bulk to the surface. However, the Pd varies oppositely, implying the opposite direction of diffusion. Note that the graph reflects the relative variations of components, not the absolute concentrations. Unlike Pd, the percentage increase of Ni from 500 to 250 nm results from the relative depletions of Cu and P. Even though the variation trend of Ni seems similar to that of Pd, we cannot conclude that they diffuse in the same direction. From 200 nm deep to the surface, there is a rapid rise of Ni above its original percentage of 10%, which means abundant Ni atoms transferred to the surface. Therefore, the diffusion directions of Ni, Cu, and P are the same, whereas that of Pd is exactly the reverse, as labeled in Figs. 3(a)–3(d). Furthermore, the sublimation effect of P may lead to the depletion of P near the surface, which has also been observed in other MGs [34].

Though the quantitative explanation of the structural difference in the binary sublayers is not yet available, a qualitative hint for understanding the structural modulation can be revealed by the elemental mapping of Fig. 3(b). Even though the sizes and diffusivities of Cu and Ni are comparable [35], the aggregation behavior of Ni is much more significant than Cu in the crystalline region. The reported studies demonstrated that monodisperse Ni nanoparticles can self-assembly organize into a superlattice because of the ferromagnetic attraction behavior of metal

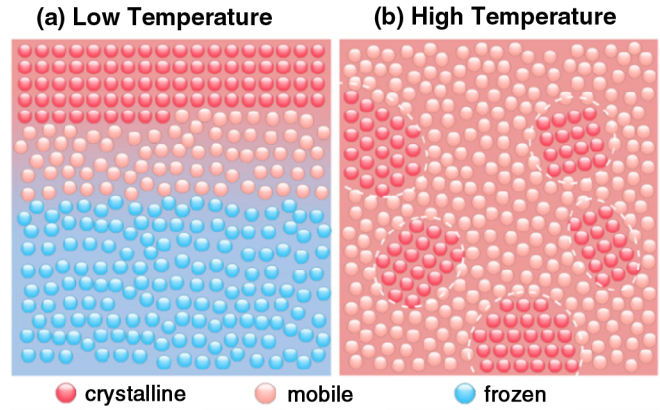


FIG. 5. The formation schematic of (a) surface superlattice-like nanostructure; (b) polycrystals. The red, pink, and blue balls represent crystalline, mobile, and frozen atoms, respectively.

Ni [36,37]. Considering the multiple components in MG, the significant aggregation confirms the stronger attraction of Ni-Ni, and the intricate competing interactions between Ni-Ni and other interparticles could account for the periodic changes of atomic array orientation, i.e., the formation of a structurally modulated nanostructure.

To investigate the temperature effect on the surface modulated structure, XRD was performed on annealed MGs at different temperatures for the same period of 200 h. Figure 4(a) shows that when elevating to 556 K, more Bragg peaks appear around the primary peak, implying the generation of new crystalline phases. The resulting cross-sectional HRTEM view [Fig. 4(b)] shows a more complicated morphology at elevated temperature, and the boundary of the surface crystalline region is no longer clear. Figure 4(c) presents the selected region of Fig. 4(b) at high magnification and manifests a misorientation of 8° between two grains, indicating that nucleation takes place simultaneously in the regions far from the surface. The crystallization peaks remain even if the surface is removed by mechanical polishing for more than $10 \mu\text{m}$ (Fig. S2 [22]), further confirming that crystallization occurs also in the interior of MG with elevating temperature. The comparative experiments confirm that the formation of a surface modulated nanostructure is sensitive to the annealing temperature near T_g .

We propose an interpretation for the growth of the surface superlattice nanostructure as illustrated in Fig. 5. Because the surface of MG is liquidlike below T_g , whereas the diffusion beneath is extremely slow and the surface energy barrier is approximately half of the bulk in MG [4,5,8], the nucleation sites preferentially initiate at the free surface and develop into a quasi-two-dimensional crystalline layer. Concomitantly, the original surface of MG is replaced, which is equivalent to a highly ordered continuous substrate at the beginning of the epitaxial growth method. Subsequently, similar to the epitaxy, the mobile atoms in the contiguous liquidlike surface region are more

likely to grow layer by layer along the surface and result in the single-crystal-like nanostructure. On the contrary, while elevating the annealing temperature approach or above T_g , the differences between the surface and bulk become smaller, and the whole glass system is unfrozen and flows simultaneously, which leads to homogeneous nucleation in the system and the formation of polycrystals. The simple schematic illustration clarifies the relationship between the fast surface dynamic and the structural characteristics of the crystallization products. Compared with the conventional epitaxial growth method, one remarkable advantage of our case is that the fabrication of a single-crystal-like structure is not confined by the substrate [38], and the only parameter to tune for searching the suitable epitaxial growth environment is a proper temperature near T_g . This work might provide insights into the surface dynamics and the crystallization mechanism in MGs and pave a simple path for fabricating unique and sophisticated nanostructure, which is possible to produce metallic composites with more excellent mechanical and functional properties and advance the MGs for practical applications.

We thank L. H. Yang, S. L. Zuo, D. Q. Zhao, and B. B. Wang for experimental assistance and discussions. This work was supported by the National Natural Science Foundation of China (Grants No. 51571209 and No. 51461165101), the 973 Program of Ministry of Science and Technology of the People's Republic of China (Grant No. 2015CB856800), and the Key Research Program of Frontier Sciences, Chinese Academy of Sciences (Grant No. QYZDY-SSW-JSC017).

L. C. and C. R. C. contributed equally to this work.

*Corresponding author.

panmx@iphy.ac.cn

†Corresponding author.

whw@iphy.ac.cn

- [1] K. S. Nakayama, Y. Yokoyama, T. Sakurai, and A. Inoue, *Appl. Phys. Lett.* **90**, 183105 (2007).
- [2] S. Sohn, Y. Jung, Y. Xie, C. Osuji, J. Schroers, and J. J. Cha, *Nat. Commun.* **6**, 8157 (2015).
- [3] T. Li, D. Donadio, L. M. Ghiringhelli, and G. Galli, *Nat. Mater.* **8**, 726 (2009).
- [4] J. D. Stevenson and P. G. Wolynes, *J. Chem. Phys.* **129**, 234514 (2008).
- [5] C. R. Cao, Y. M. Lu, H. Y. Bai, and W. H. Wang, *Appl. Phys. Lett.* **107**, 141606 (2015).
- [6] L. Zhu, C. W. Brian, S. F. Swallen, P. T. Straus, M. D. Ediger, and L. Yu, *Phys. Rev. Lett.* **106**, 256103 (2011).
- [7] S. Capaccioli, K. L. Ngai, M. Paluch, and D. Prevosto, *Phys. Rev. E* **86**, 051503 (2012).
- [8] Y. Chai, T. Salez, J. D. McGraw, M. Benzaquen, K. Dalnoki-Veress, E. Raphael, and J. A. Forrest, *Science* **343**, 994 (2014).
- [9] Z. Fakhraai and J. A. Forrest, *Science* **319**, 600 (2008).
- [10] S. F. Swallen, K. L. Kearns, M. K. Mapes, Y. S. Kim, R. J. McMahon, M. D. Ediger, T. Wu, L. Yu, and S. Satija, *Science* **315**, 353 (2007).
- [11] H. B. Yu, Y. Luo, and K. Samwer, *Adv. Mater.* **25**, 5904 (2013).
- [12] L. Zhu, L. Wong, and L. Yu, *Mol. Pharmaceutics* **5**, 921 (2008).
- [13] M. Hasebe, D. Musumeci, and L. Yu, *J. Phys. Chem. B* **119**, 3304 (2015).
- [14] R. Stephens, *J. Appl. Phys.* **51**, 6197 (1980).
- [15] J. Sallèse, A. Ils, D. Bouvet, P. Fazan, and C. Merritt, *J. Appl. Phys.* **88**, 5751 (2000).
- [16] M. Ashby and A. Greer, *Scr. Mater.* **54**, 321 (2006).
- [17] W. H. Wang, *Adv. Mater.* **21**, 4524 (2009).
- [18] T. Egami, *Prog. Mater. Sci.* **56**, 637 (2011).
- [19] W. H. Wang, *Prog. Mater. Sci.* **57**, 487 (2012).
- [20] G. Kumar, A. Desai, and J. Schroers, *Adv. Mater.* **23**, 461 (2011).
- [21] G. Doubek, R. C. Sekol, J. Li, W. H. Ryu, F. S. Gittleson, S. Nejati, E. Moy, C. Reid, M. Carmo, and M. Linardi *et al.*, *Adv. Mater.* **28**, 1940 (2016).
- [22] See the Supplemental Material at <http://link.aps.org/supplemental/10.1103/PhysRevLett.118.016101> for experimental details and additional information.
- [23] X.-P. Tang, U. Geyer, R. Busch, W. L. Johnson, and Y. Wu, *Nature (London)* **402**, 160 (1999).
- [24] M. Wollgarten, S. Mechler, E. Davidov, N. Wanderka, and M.-P. Macht, *Intermetallics* **12**, 1251 (2004).
- [25] N. Wanderka, E. Davidov, G. Mieke, V. Naundorf, M.-P. Macht, and J. Banhart, *J. Metastab. Nanocryst. Mater.* **20**, 35 (2004).
- [26] D. B. Williams, *Transmission Electron Microscopy: A Textbook for Materials Science* (Springer, New York, 2009).
- [27] L. Wang, W. Wang, L. Sun, J. Zhao, D. Dai, and W. Wang, *Sci. China, Ser. B: Chem., Life Sci., Earth Sci.* **43**, 407 (2000).
- [28] M. A. Gibson and G. W. Delamore, *J. Mater. Sci.* **23**, 1164 (1988).
- [29] H. S. Chen, L. C. Kimerling, J. M. Poate, and W. L. Brown, *Appl. Phys. Lett.* **32**, 461 (1978).
- [30] A. Seiffodini and S. Zaremehrdardi, *J. Non-Cryst. Solids* **432**, 313 (2016).
- [31] A. A. Tsarkov, E. N. Zanaeva, A. Y. Churyumov, S. V. Ketov, and D. V. Louzguine-Luzgin, *Mater. Charact.* **111**, 75 (2016).
- [32] D. Savytskii, B. Knorr, V. Dierolf, and H. Jain, *Sci. Rep.* **6**, 23324 (2016).
- [33] P. Venezuela, J. Tersoff, J. A. Floro, E. Chason, D. M. Follstaedt, F. Liu, and M. G. Lagally, *Nature (London)* **397**, 678 (1999).
- [34] H.-G. Wagner, M. Ackermann, R. Goa, and U. Gonser, in *Rapidly Quenched Metals*, edited by S. Steeb and H. Warlimont (North-Holland, Amsterdam, 1985), p. 247.
- [35] M. Chathoth, A. Meyer, M. Koza, and F. Juranyi, *Appl. Phys. Lett.* **85**, 4881 (2004).
- [36] C. Murray, S. Sun, H. Doyle, and T. Betley, *MRS Bull.* **26**, 985 (2001).
- [37] J. Park, E. Kang, S. U. Son, H. M. Park, M. K. Lee, J. Kim, K. W. Kim, H. J. Noh, J. H. Park, and C. J. Bae, *Adv. Mater.* **17**, 429 (2005).
- [38] J. J. de Miguel and R. Miranda, *J. Phys. Condens. Matter* **14**, R1063 (2002).